# Effect of heat release on turbulence and scalar-turbulence interaction in premixed combustion

G. Hartung,[1] J. Hult,[1] C. F. Kaminski,[1] J. W. Rogerson,[2] and N. Swaminathan[2,a)]
[1]*Department of Chemical Engineering, University of Cambridge, Cambridge CB2 3RA, United Kingdom*
[2]*Department of Engineering, University of Cambridge, Cambridge CB2 1PZ, United Kingdom*

(Received 18 July 2007; accepted 12 February 2008; published online 25 March 2008)

Stereoscopic particle image velocimetry and planar laser induced fluorescence measurements of hydroxyl radical are simultaneously applied to measure, respectively, local turbulence intensities and flame front position in premixed ethylene-air flames stabilized on a bluff body. Three different equivalence ratios, 0.55, 0.63, and 0.7, and three different Reynolds numbers, 14 000, 17 000, and 21 000, are considered. Laser measurements were made for five different flame configurations within the ranges above and in the corresponding cold flows. By comparing the measurements of the cold and the corresponding hot flows, the effect of heat release on the turbulence and its interaction with the flame front is studied. All the flames are in the thin reaction zone regime. Typical flow features forming behind the bluff body are observed in the cold flows, whereas in the reacting flows the mean velocities and thus the shape, size, and characteristics of the recirculating eddy behind the bluff body are strongly influenced by the heat release. The strong acceleration across the mean flame and the radial outward shift of the stagnation plane of the recirculating eddy yield negative radial velocities which are absent in the corresponding cold flow cases. The spatial intermittency of the flame front leads to an increase in the turbulent kinetic energy. Although a decrease in the mean and rms values of the strain rate tensor $e_{ij}$ components is observed for the reacting case as one would expect, the local flow acceleration across the flame front leads to a substantial increase in the skewness and the kurtosis of the probability density functions (PDFs) of $e_{ij}$ components. The turbulence-scalar interaction is studied by analyzing the orientation of the flame front normal with the eigenvectors of $e_{ij}$. The PDFs of this orientation clearly show that the normals have an increased tendency to align with the extensive strain rate, which implies that the scalar gradients are destroyed by the turbulence as the scalar isosurfaces are pulled apart. This result questions the validity of passive scalar turbulence physics commonly used for premixed flame modeling. However, the influence of Lewis number on this alignment behavior is not clear at this time. © *2008 American Institute of Physics*. [DOI: 10.1063/1.2896285]

## I. INTRODUCTION

The modeling of turbulent premixed flames requires scalar gradient information in one form or another. For example, the flame surface density is closely related to the local scalar gradient. In other approaches such as flamelets,[1] conditional moment closure,[2] and joint probability density function[3] (PDF) the required scalar gradient information comes via either the mean or the conditionally averaged scalar dissipation rate. The instantaneous scalar dissipation rate is defined as $N_c \equiv \kappa(\nabla c \cdot \nabla c) = \kappa(\partial c/\partial x_i)$,[2] where $c$ is a reaction progress variable and $\kappa$ is its diffusivity. In the mixing controlled limit, the mean[4] as well as the instantaneous[5] reaction rate have direct dependence on the scalar dissipation rate. Thus, one can clearly see the central role played by the scalar dissipation rate in turbulent flame calculations.

An exact transport equation for the scalar dissipation rate proposed recently[6] identifies the influences of chemical reaction, dilatation, and the interaction of turbulence with chemical reaction and scalar mixing on the evolution of $N_c$. This equation, in the usual nomenclature, is written as

$$\rho\frac{DN_c}{Dt} = \frac{\partial}{\partial x_j}\left(\rho\kappa\frac{\partial N_c}{\partial x_j}\right) - 2\rho\kappa\kappa\left[\frac{\partial}{\partial x_j}\left(\frac{\partial c}{\partial x_i}\right)\right]^2 - 2\rho\kappa\frac{\partial c}{\partial x_i}e_{ij}\frac{\partial c}{\partial x_j} + 2\rho N_c\left(\frac{\partial u_l}{\partial x_l}\right) + 2\kappa\frac{\partial c}{\partial x_i}\frac{\partial \dot{\omega}}{\partial x_i}, \quad (1)$$

where the molecular diffusivity $\kappa$ has a weak dependence on temperature. The fluid density is denoted by $\rho$ and the strain rate is $e_{ij} \equiv 0.5(\partial u_i/\partial x_j + \partial u_j/\partial x_i)$ with $u_i$ as the velocity in the spatial direction $x_i$. The left hand side of Eq. (1) represents the temporal and convective changes of $N_c$. The first term on the right hand side is the diffusive flux. The second term is the dissipation of the scalar gradient due to the molecular dissipation. The third term is the turbulence-scalar interaction. The fourth term originates from chemical and diffusive processes undergone by $c$. This term appears because of dilatation across the flame front. Since $c$ is a reactive scalar, the fifth term is the usual production of $N_c$ because of chemical reaction.

Here, the interest is on the turbulence-scalar interaction term represented by $[(\partial c/\partial x_i)e_{ij}(\partial c/\partial x_j)]$. This term signifies the production or dissipation of scalar gradients by the action of turbulence. The production of scalar gradients will result

a)Author to whom correspondence should be addressed. Electronic mail: ns341@cam.ac.uk.

 

when the gradient vector preferentially aligns with the most compressive principal strain rate as has been observed in a number of earlier studies.[7–14] However, the generality of the above alignment when the flow involves additional physics such as strong rotation has been questioned recently.[15] The presence of passive chemical reactions does not alter the above alignment.[16,17] It has been shown recently[18] that the scalar gradient vector has an increased tendency to align with the most extensive principal strain rate when the chemical reactions are nonpassive. This preferential alignment was observed at almost all locations inside the flame brush when the Damköhler number is large. For small values of Damköhler number, the alignment with the extensive strain rate was observed in the regions of intense heat release.[19] The Damköhler number Da is defined as the ratio of large scale turbulence time, $\Lambda/u'$, to the characteristic flame time, $\delta_L^o/s_L^o$. The rms of turbulence velocity fluctuations and its integral length scale are denoted by $u'$ and $\Lambda$, respectively. The thermal thickness of an unstrained laminar flame and its propagation speed are denoted by $\delta_L^o$ and $s_L^o$, respectively.

The preferential alignment with the most extensive principal strain rate results in the dissipation of scalar gradient by the turbulence, which is contrary to the classical picture where the production of the scalar gradient by the turbulence results because of its alignment with the most compressive principal strain rate. This change in the behavior observed via direct numerical simulation (DNS) has profound implication on turbulent combustion model development.[20] The DNS studies[18–20] used turbulent flames having high and low Da. The high Da flame also had $\mathrm{Ka}<1$, while the low Da flame had $\mathrm{Ka}>1$, where Ka is the Karlovitz number which is defined as the ratio of characteristic flame time to the Kolmogorov time. This dimensionless number represents the competition between chemical and fluid dynamic processes of small scales and it is defined as

$$\mathrm{Ka}=\frac{\delta^2}{\eta^2}=\frac{t_c}{t_\eta}, \tag{2}$$

where $\delta \equiv \kappa/s_L^o$ is the Zeldovich thickness and $\eta$ is the Kolmogorov length scale. The Zeldovich and thermal thicknesses are approximately related[6] to each other via $\delta_L^o/\delta = 2(1+\tau)^{0.7}$, where $\tau$ is the heat release parameter defined later. The characteristic chemical time scale is $t_c$ and the Kolmogorov time scale is $t_\eta$. Now, it is apparent that the DNS flames[18,19] had the characteristic flame scales to be either smaller, in $\mathrm{Da}>1$ and $\mathrm{Ka}<1$ case, or larger, in the $\mathrm{Da}<1$ and $\mathrm{Ka}>1$ case, than all the relevant turbulent scales. Here, the interest is to understand the turbulence-scalar interaction in premixed flames with $\mathrm{Da}>1$ and $\mathrm{Ka}>1$. These flames are called intermediate Da flames and according to Peters,[21] they are classified to be in the thin reaction zone regime of turbulent combustion. It is likely that the flames in practical devices will have the attributes of the intermediate Da regime; the flame scales are smaller than the typical large scales of turbulence and the flame scales are larger than the relevant small scales of turbulence. Directly simulating turbulent flames with this attribute are computationally demanding, and hence we resort to laboratory experiments here. The specific objectives for this study are the following:

(1) To conduct laboratory experiments of turbulent premixed flames with the above attributes and to apply sophisticated laser diagnostic techniques to carefully measure all three components of the velocity field, flame front location, its curvature, and fluid dynamic strain rates, if possible, $e_{ij}$.
(2) To elucidate the effect of heat release on various mean turbulence quantities such as integral length scale, rms velocity, PDFs of $e_{ij}$ components, etc.
(3) To investigate turbulence-scalar interaction by studying the alignment of flame normal with the principal strain rates.

The mean quantities can be used to compare and validate the numerical simulation results and the combustion submodels. Here, our prime aim is to study the turbulence-scalar interaction in premixed flames with $\mathrm{Da}>1$ and $\mathrm{Ka}>1$.

In the next section, the experimental setup and methodology used to achieve the above objectives are described. The results are presented and discussed in Sec. III and the conclusions are summarized in the final section.

## II. EXPERIMENTAL METHODS

In this section, the burner used in the experiments, the conditions of turbulent premixed flames studied, the measurement techniques and the data reduction methods employed are described briefly. A more complete description can be found elsewhere.[22] The measurements reported here are obtained by simultaneously employing stereoscopic particle image velocimetry (SPIV), which provides all three components of the velocity field in a plane intersecting the flame and time-sequenced OH-planar laser induced fluorescence (OH-PLIF) which allowed the flame front to be tracked. The justification for the use of OH-PLIF is given later.

### A. Burner and flame characteristics

The 10 kW burner used in this study has a simple construction as illustrated in Fig. 1 and it has been employed in earlier studies.[23–25] This burner is similar to that used by Heitor *et al.*[26] but the flow and flame conditions investigated here are different. The burner was made up of a circular duct, 300 mm long with an inner diameter of 35 mm. An inverted conical bluff-body having a diameter of 25 mm and giving a blockage ratio of 50% is used, as shown in Fig. 1, to stabilize the turbulent flame. This figure also shows the coordinate system used to present the results in Sec. III. The premixed ethylene-air mixture of a given equivalence ratio $\Phi$ enters the plenum chamber at the bottom and flows upward through the flow conditioners and exits through the annular gap surrounding the central bluff body. The two loudspeakers, mounted diametrically opposite to each other, are an integral part of the plenum chamber and they are installed to allow acoustic forcing to be imposed on the flow. However, the speakers were inactive for this study. A complete description of the burner and its characterization can be found in Ref. 25.

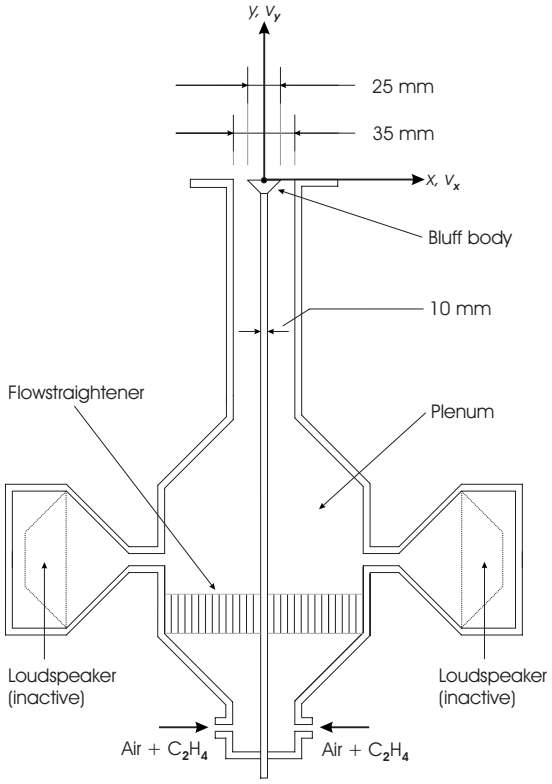


FIG. 1. Schematic of bluff body burner used in this study.

The flow and flame conditions investigated in this study are tabulated in Table I. Two sets of experiments were conducted. In one set the reactant mixtures were not ignited and thus the flow is cold. In the second set of experiments the mixtures having the same flow conditions as in the cold flow cases were ignited. The effect of heat release on the turbulence quantities can be studied by comparing the results from these two sets of experiments. The turbulent flame, referred to as FA listed in Table I, has an equivalence ratio of $\Phi = 0.55$ and three different values of Reynolds number Re based on the bulk mean velocity $U_b$ at the exit of the burner, the hydraulic diameter of the annular exit and the kinematic viscosity of the cold ($T_u = 288$ K) reactant mixture. These three values are Re= 14 000, 17 000, and 21 000 as given in Table I. The flames denoted as FB1 and FC1 had the same Re number as FA1 but different equivalence ratios: $\Phi = 0.63$ and 0.70, respectively. These three flames have Le $\simeq 1.0$, where Le is the Lewis number defined as the ratio of thermal diffusivity to mass diffusivity. The heat release parameter is defined as $\tau \equiv (T_b - T_u)/T_u$, where $T$ is the absolute temperature and the subscripts $b$ and $u$, respectively, denote burnt and unburnt mixtures of a planar laminar flame. The planar laminar flame speed $s_L^o$ and the burnt side temperature were obtained from the literature,[27,28] and thermal thickness was calculated using the Zeldovich thickness as noted in the Introduction section. The values of Damköhler and Karlovitz numbers averaged over the imaging plane are denoted by $\overline{\mathrm{Da}}$ and $\overline{\mathrm{Ka}}$ in Table I and more details on these two parameters will be given later in Sec. III. At this stage, it is to be noted that $\overline{\mathrm{Da}} > 1$ and $\overline{\mathrm{Ka}} > 1$, and thus these flames are expected to be in the thickened flame regime or thin reaction zone regime of turbulent combustion. This point will also become more apparent in Sec. III.

### B. Laser diagnostics

Diagnostics used in this study were centered around the application of planar LIF measurements of OH in conjunction with stereoscopic PIV measurements to identify the flame front contour and velocity fields. For the results reported here, a high spatial resolution and good signal to noise ratio were essential to obtain the necessary gradient information.[29–31] There is continuing debate on the usefulness of OH as a flame front marker in turbulent combustion, owing to its persistence after its production which can lead to misinterpretations concerning the reaction zone location.[32] Other species such as CH,[33,34] CH2O,[35] the product of CH2O and OH LIF images,[36,37] etc., have been used in the past as flame front markers to study turbulent flames. However, all of these methods offer inferior signal to noise ratios and thus reduced data fidelity. We have performed extensive validation studies on the flame reported here, using simultaneous CH2O and OH PLIF imaging, reaction rate, and thermometry imaging.[22–24] These studies demonstrated that the isocontour of maximum OH gradient is an accurate marker for the flame front position over the conditions studied here. The real advantage, however, is the superior signal to noise ratio obtained with the latter, permitting gradient information to be extracted with confidence and simultaneous application of PIV with high fidelity in burnt, unburnt, and reacting regions simultaneously.

#### 1. OH-PLIF

Figure 2 shows a schematic of the diagnostic set-up employed for the combined OH-PLIF and SPIV measurements. The diagnostic system for OH-PLIF consisted of one Nd:YAG laser (Continuum Surelite II) pumping a tunable dye laser (Sirah Cobra-Stretch) and a high-resolution ICCD

TABLE I. Flow and flame conditions investigated.

| Flames | $\Phi$ | $U_b$(m s$^{-1}$) | Re | $\tau$ | $\delta_L^o$($\mu$m) | $s_L^o$(m s$^{-1}$) | $\overline{\mathrm{Da}}$ | $\overline{\mathrm{Ka}}$ |
|---|---|---|---|---|---|---|---|---|
| FA0 | 0.55 | 8.1 | 14 000 | 4.83 | 512 | 0.20 | 1.69 | 5.93 |
| FA1 | 0.55 | 9.9 | 17 000 | 4.83 | 512 | 0.20 | 1.37 | 7.58 |
| FA2 | 0.55 | 12.7 | 21 000 | 4.83 | 512 | 0.20 | 1.00 | 13.76 |
| FB1 | 0.63 | 9.9 | 17 000 | 5.34 | 385 | 0.28 | 2.44 | 4.13 |
| FC1 | 0.70 | 9.9 | 17 000 | 5.58 | 307 | 0.36 | 4.01 | 2.40 |

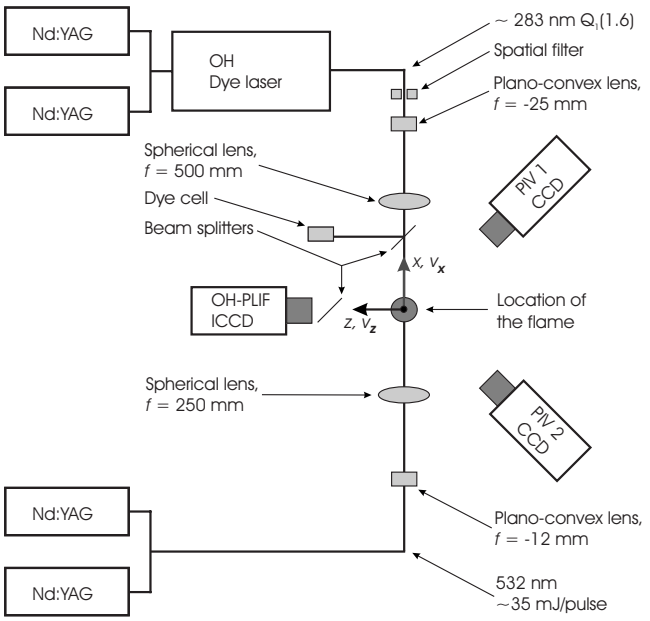


FIG. 2. Laser and optical setup for combined OH-PLIF and SPIV measurements employed in this study.

camera (Nanostar, Lavision), which was used to image the OH-PLIF signal. The camera intensifier was synchronized to the laser source and was gated to open for 350 ns for the PLIF measurements. It was fitted with a UV-transmitting $f/4.5$ camera lens (Nikkor) equipped with UG 11 and WG 305 filters (Comar). For spectral identification of the OH transitions, a LIF excitation scan was performed prior to the PLIF measurements. For OH-LIF, the frequency-doubled output from the dye laser was tuned near 283 nm to excite the $Q_1(6)$ line in the $A\,^2\Sigma^+$-$X\,^2\Pi(1,0)$ band. Pulse energies of 8 mJ were available from the dye laser, but the beam was spatially filtered yielding a measured irradiance of $\sim 1.3\ \mathrm{MW/cm^2\,cm^{-1}}$ in the measurement region. The laser output had a linewidth of $0.12\ \mathrm{cm^{-1}}$ was expanded into a sheet of 50 mm high and 100 $\mu$m thick, using a cylindrical planoconvex lens with a focal length of $f=-25$ mm and spherical lens with focal length of $f=+500$ mm. A region of 5 cm wide and 4 cm high was imaged. The spatial intensity profile of the laser sheet was measured on a pulse-to-pulse basis simultaneously with the PLIF signal. As shown in Fig. 2, part of the focused light sheet was directed into a dye cell, which was filled with an aqueous solution of a fluorescent dye. The dye cell was positioned in such a way that the PLIF signal as well as the fluorescent dye were in focus on the ICCD chip. The dye fluorescence was imaged onto a strip of approximately 100 pixels in width to one side of the ICCD chip to provide an instantaneous beam power profile measurement.

### 2. Stereoscopic PIV

Stereoscopic PIV was performed to characterize the velocity fields of both unburnt and burnt gases above the burner. The second harmonic from a pulsed double-cavity Nd:YAG laser (Big Sky Laser Technologies Inc., Ultra 1, 35 mJ/pulse) was used to create a light sheet of 480 $\mu$m thickness [full width at half maximum (FWHM)]. The PIV lasers and PIV cameras were triggered from a PIV synchronizer (ILA, Germany) which in turn was triggered from a waveform generator (TGA 1242, TTi, UK). Two PIV cameras (Sensicam, PCO imaging, Germany, 1280 $\times$ 1024 pixels, double frame mode) were arranged at 90° with the lenses arranged according to the Scheimpflug criterion. Each camera was fitted with a narrow bandpass interference filter (centered at 532 nm with 10 nm FWHM; maximum transmission=90%) to reject flame emission. The separation between the PIV laser pulses was 15 $\mu$s. This time spacing corresponds to a particle displacement between 0 and 8 pixels. $SiO_2$ particles with a primary diameter of 12 nm (Aerosil R 812, Degussa, Germany) were seeded into the reactive mixture with a fluidized bed followed by a cyclone and a choke to select only the smallest particles with a diameter less than 1 $\mu$m and to dissociate large agglomerates. The PIV laser sheets were overlapped with the OH-PLIF sheets in a counterpropagating configuration, as shown in Fig. 2. A sequence of image collection was started with an OH-PLIF image ($t=0$ $\mu$s). A delay of 500 ns was set between the OH-PLIF image and the first PIV image ($t=0.5$ $\mu$s) to avoid potential interferences between the laser pulses and cameras. At the given bulk velocities and with the spatial resolution of the optical setup, the delay of 500 ns employed between the pulses rendered these measurements virtually instantaneous on flow timescales.

The DAVIS 7.1 processing software (Lavision, Germany) was used for velocity calculations. After subtracting the minimum intensity level in each double frame image, the data were cross correlated at successively smaller interrogation regions leading to a discrete window offset.[38] After each path the peak ratio of the highest to the second highest peak from the cross correlation (peak ratio: 1.8) and the change of velocity with respect to the standard deviation were used to remove invalid vectors and to interpolate between them. The final cross correlation employed an interrogation region of $8\times8$ pixels, which corresponds to $274\times274$ $\mu$m. Finally, the two velocity fields extracted from the two individual cameras were combined to yield a three-component velocity field. On average more than 98% valid vectors were obtained in the particle seeded field of view. A $3\times3$ Gaussian smoothing operation was carried out in the cases when derivatives were calculated. One of several advantages of using stereoscopic PIV is that regions of strong three-dimensional (3D)-flow character can be directly identified.

## C. Data reduction technique

### 1. Mapping of scalar and velocity fields

The PLIF image and PIV image were first aligned and superimposed on a pixel-by-pixel basis. This alignment is essential to the success of these imaging techniques because of the small spatial scales of reacting layers in the flame. The mapping procedure was performed in several stages. First, both laser sheets were aligned to pass through the exactly same measurement plane. Then, a target image (cross pattern) was positioned in the measurement plane at the exact position of the laser sheets and in the view of all three cam-

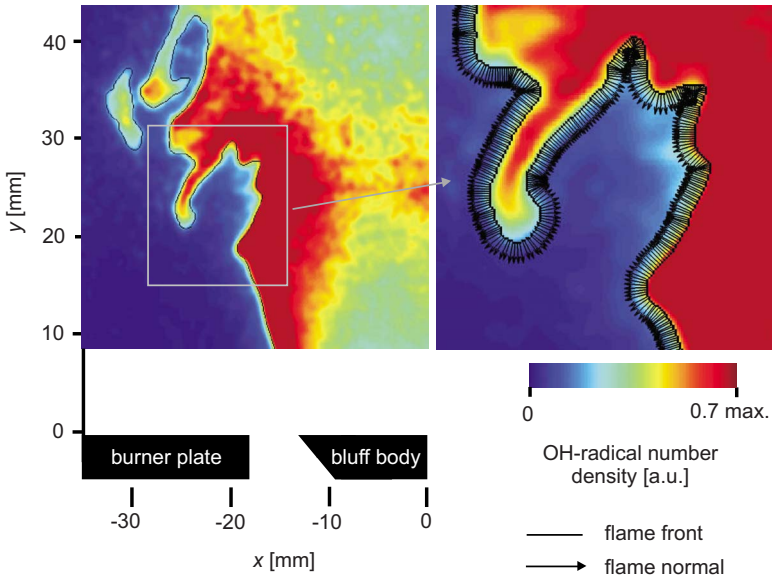


FIG. 3. (Color online) Illustration of flame normals represented by black vectors. The flame front corresponds to the line of maximum gradient in the OH-radical concentration and subdivides the OH-field into burnt and unburnt regions. The image is shown for the flame FC1.

eras. The coordinates of 90 reference points on the target image were captured by both PIV cameras, dewarped in the PIV software (LAVISION), and both images superimposed (image A). The PLIF image (image B) taken of the same target was mirrored and the corresponding coordinates of the 90 reference points were identified. The coordinates of image B were then mapped onto image A, using a transformation matrix relating the two sets of coordinates to each other. The precision of this procedure is in the subpixel range.[39] These operations reduced the OH-pixel resolution by 6% from 86 to 92 $\mu$m. The vector field was finally enlarged by a factor of 3 in a bicubic interpolation scheme to match the matrix size of the OH field.

### 2. Extraction of flame front

Information on flame front position are derived from OH-PLIF images as follows. First a background image, measured in the absence of the flame, was subtracted from the fluorescence images. These images were then corrected for laser sheet inhomogeneities using the instantaneous laser power profile recorded with each image. As part of this procedure any stretch, rotation, and vertical shifts between the instantaneous power profile image and the OH image were corrected for. An anisotropic nonlinear diffusion filter was applied[40] to reduce the level of noise and to enhance gradients in the images. The images were resized to 50% of their original size after filtering which yields a signal to noise ratio gain of around 4. The flame contours, identified by the maximum gradient in the OH field, were then located using a Canny edge detection algorithm.[41] The images were then binarized into unburnt and burnt regions along the maximum gradient. This procedure was found to yield the flame contour more consistently than using the commonly employed constant threshold algorithm. Furthermore, detailed analyses of laminar flame results obtained using PREMIX code[42] showed that the location of the maximum gradient of OH coincided with the location of the maximum in the product of OH and CH2O concentrations. This implies that the contour of the maximum OH gradient is located inside the intense heat releasing regions, which are marked by the product of OH and CH2O concentration, and it marks the flame front precisely. In the latter approach, the images are binarized into unburnt and burnt regions with the interface between these regions taken to be the flame front location. The drawback of this method is that the signal to noise ratio of the images can vary widely both due to beam profile inhomogeneities and to variations in OH concentration (see Fig. 3). In the present configuration it was observed that this led to uncertainties of up to 10 pixels, which was too large for a meaningful statistical analysis of the alignment of the principal strain rates and the flame normal.

An arbitrary single shot OH-PLIF image for flame FC1 is shown in Fig. 3. The flame front contour is also superimposed as a black line and follows along the line of maximum gradient of the OH concentration. An important point to note is that the OH intensity at the location of the flame front shows a large variation along the flame contour. Some extreme cases having high and low OH concentrations at the flame front are also visible in Fig. 3. Also, it is to be noted that the size of the imaging plane in the reacting case is reduced by about 6% to increase the effective resolution.

### 3. Flame curvature and its normal

For the calculation of flame curvature and its normal, the pixels marking the flame front were sorted to a connected pixel line with coordinates $x$ and $y$. A local coordinate $s$ was introduced whose magnitude increased along the connected pixel line by the distance between adjacent pixel locations. In order to analytically describe the flame contour,[43] two third order polynomials $f_x(s)$ and $f_y(s)$ were fitted along the flame as a function of $s$ using 7 pixels on either side of the center pixel. The analytical expression thus obtained was then used to calculate the curvature $k$ for each pixel along the sorted line of the flame front pixels using the following formula:[44]

$$k = \left[ \frac{df_x}{ds}\frac{d^2f_y}{ds^2} - \frac{d^2f_x}{ds^2}\frac{df_y}{ds} \right] \left[ \left( \frac{df_x}{ds} \right)^2 + \left( \frac{df_y}{ds} \right)^2 \right]^{-1.5}. \quad (3)$$

The same analytical expressions were also used to determine the flame normal; $n_x = df_x/ds$ and $n_y = df_y/ds$. A typical OH-PLIF image is depicted in Fig. 3. For the window highlighted in gray, the flame normals are plotted for each pixel of the flame front. As can be seen from this figure, the normals obtained, both for locations with high and low curvatures are accurate. The flame curvature as well as its normal was calculated for all flame front elements appearing in each OH-PLIF image.

#### 4. Two dimensional (2D) measurements of 3D flow

It is not possible to completely characterize the flow as 2D measurements (PLIF and SPIV) are employed to gain information on a 3D flow. However, as it was discussed in Sec. II A, the flame is axis symmetric on an average. For $v_z > 2$ ms$^{-1}$ convection of large scale structures into and out of the measurement plane were observed. This can cause an "artificial" flame front displacement leading to a bias in the evaluated strain probability density plots. Thus, the statistical analyses of velocity and flame front information were not carried out for regions where the out-of-plane velocity component $v_z$ is larger than 2 ms$^{-1}$. The velocity fields obtained as above are differentiated using *Richardson extrapolation* scheme, since this scheme combines high accuracy with reasonable precision.[45] These velocity gradients allows us to form a $2 \times 2$ strain tensor matrix. The eigenvalues and eigenvectors of this matrix at every pixel give the principal strain rates and their directions, respectively. It is to be noted that there are only two principal strain rates; one is compressive and the other one is extensive.

### D. Resolution and accuracy

We estimate the uncertainty of our velocity data to be very similar to the uncertainties reported by Mullin and Dahm,[46,29] as their experimental setup and conditions closely resemble those employed here. The uncertainty they report is 6.5% for the in-plane velocity components $v_x$ and $v_y$ and 10.5% for the out-of-plane velocity component $v_z$. Mullin and Dahm obtained those uncertainty estimates by illuminating an identical measurement plane with a dual-color stereoscopic system. We follow this approach since we are convinced that this is the most objective way to assess the uncertainty of velocity data obtained from PIV measurements. Subjecting the velocity data from PIV to a Gaussian smoothing $(3 \times 3, \sigma = 1)$ reduces the uncertainty of the filtered velocity data to about one-third (2.2%). The uncertainty in the subsequent calculation of the principal strain increases since the calculation of the strain field is based on the velocity gradients. A thorough error propagation analysis revealed that the uncertainty of the eigenvalues of the strain tensor peaks at a level of 14%. The same analysis also reveals that 80% of the eigenvectors have an uncertainty of 6% or less in their orientation. The uncertainty of the orientation of these eigenvectors peaks at 1.3%, as can be inferred from Fig. 4.

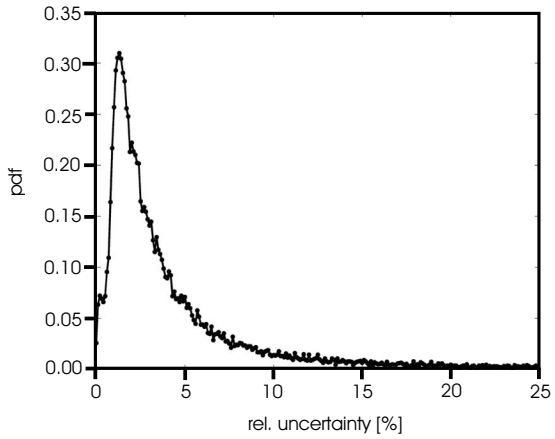


FIG. 4. PDF of relative uncertainty in the orientation of the extensive eigenvector.

## III. RESULTS AND DISCUSSION

The flow velocities and the flame front location measured using SPIV and OH-PLIF techniques as noted in the previous sections are analyzed in detail to study the turbulence-scalar interaction. Before presenting the results on the flame orientation with the principal strain rates, the effect of heat release on the fluid dynamic quantities is discussed.

### A. Effects of heat release on turbulence

#### 1. Mean flow quantities

Figure 5 shows the spatial variation of $U \equiv \sqrt{V_x^2 + V_y^2}$, $V_z$, and the root mean square (rms) of velocity fluctuations in the flame FA1 and the corresponding cold flow case. The mean velocities in $x$, $y$, and $z$ directions are denoted by $V_x$, $V_y$, and $V_z$, respectively. The cold flow results are shown in Figs. 5(a)–5(d) and the flame results are shown in Figs. 5(e)–5(h). The flame measurements were only performed from $y = 10$ and above to increase the effective resolution and to capture the details of the strongly turbulent part of the premixed flame. The mean velocities $U$ and $V_z$ depicted in Figs. 5(a), 5(b), 5(e), and 5(f) clearly show that the recirculation zone behind the bluff body is drastically influenced by heat release effects. The counter-rotating eddies are dilated and their shapes, orientations, and characteristics are strongly influenced by the heat release. This observation is consistent with an earlier investigation using laser-Doppler anemometry in a similar burner.[26] The negative $V_z$ disappears and there is a strong reduction in the shear $\partial V_z/\partial x$ in the presence of a flame. The dilation of the eddies has also been observed for bluff body stabilized turbulent nonpremixed flames.[47]

A close inspection of Figs. 5(a) and 5(e) reveals that the orientation of the mean velocity vectors has changed in the reacting case because of the strong acceleration across the flame brush and the outward shift of the stagnation plane existing between the jetlike and the recirculation regions. Because of these changes, the mean velocity in the $x$ direction, $V_x$, becomes negative which leads to the change in the direction of the velocity vector observed in Fig. 5(e). Figures

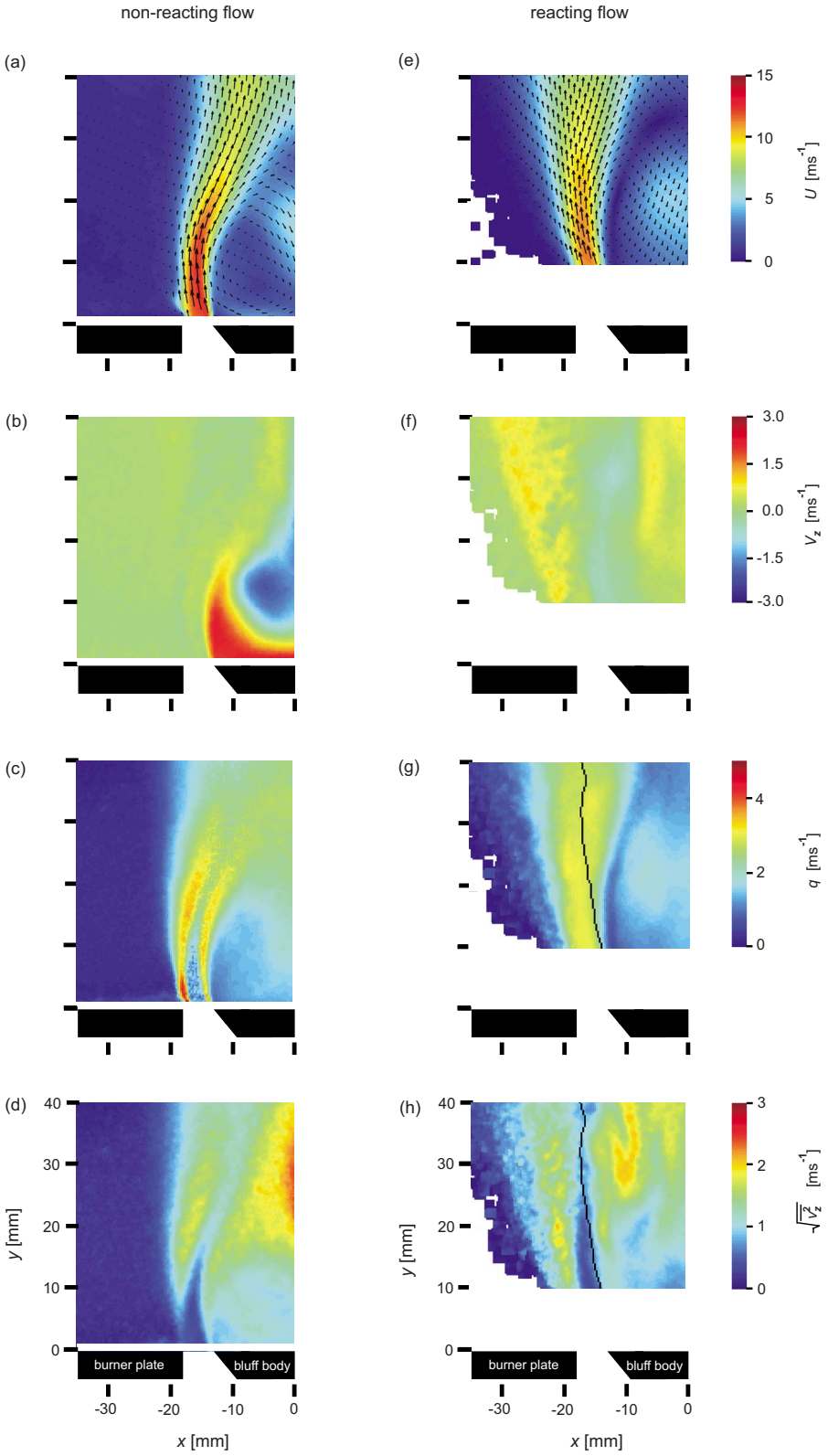


FIG. 5. (Color online) Colormap of mean velocities and rms of velocity fluctuations in nonreacting [(a)–(d)] and reacting [(e)–(h)] cases with conditions of the flame FA1. (a), (e) Mean velocity vector $U \equiv \sqrt{V_x^2+V_y^2}$ and its magnitude; (b), (f) $V_z$; (c), (g) $q \equiv \sqrt{\overline{v_x^2}+\overline{v_y^2}}$; (d), (h) rms of velocity fluctuation in $z$ direction $\sqrt{\overline{v_z^2}}$. The black lines in (g) and (h) denote the mean flame contour.

6(a)–6(c) show the variation of $V_x$, $V_y$, and $q$ along $x$ for the cases shown in Fig. 5. The profiles are shown at four different $y$ locations ($y=10$, 20, 30, and 40 mm) for nonreacting and reacting conditions. The presence of negative $V_x$ and other points discussed above are clear in Figs. 6(a) and 6(b), where the cross stream variation of $V_x$ and $V_y$ is shown. A close study of Figs. 5(a), 5(e), and 6(b) reveals that the thickness of the jetlike region is increased in the reacting case due to dilatation and the turbulence generation behind the flame. The increased thickness can also imply an increase in the entrainment rate of the ambient air, as observed by Heitor *et al.*[26] The entrainment can possibly dilute the reactant mixture in the downstream via large scale mixing. It is not possible to assess this effect within the scope of the current

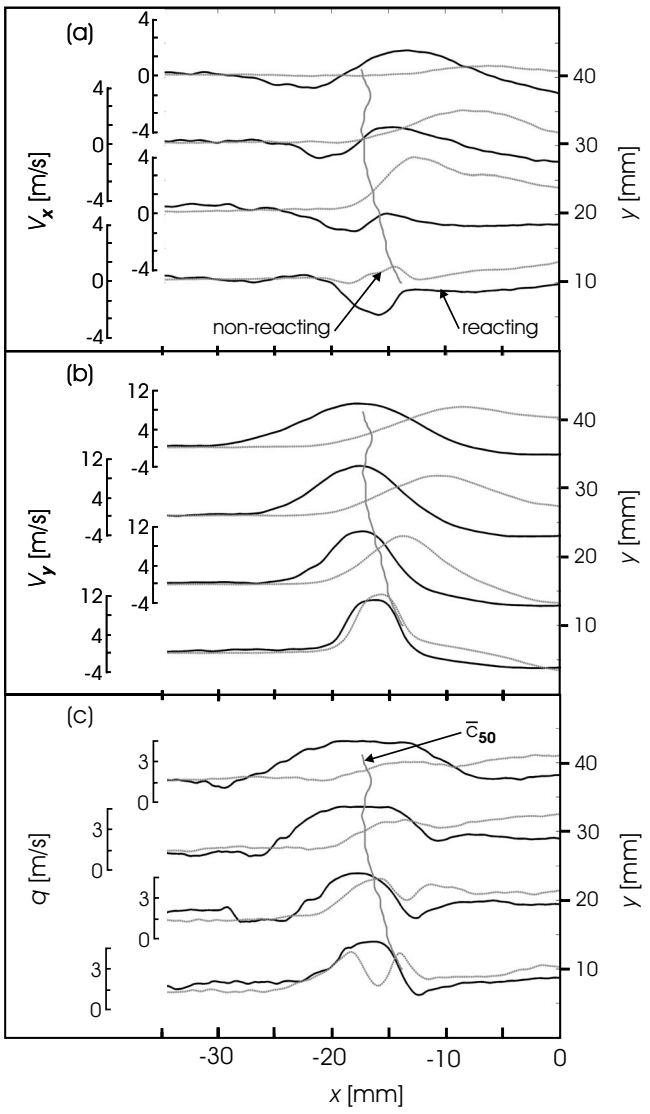


FIG. 6. The variation of (a) $V_x$, (b) $V_y$, and (c) $q$ along $x$ (across the flame brush) for the case shown in Fig. 5. The profiles are shown for four $y$ locations for both nonreacting and reacting cases. The gray line running from $y=10$ to 40 represents the mean flame contour.

diagnostics setup. Furthermore, the conclusions to be drawn on the small scale quantities are less likely to be influenced by the dilution effect.

The combined rms of velocity fluctuations, $q \equiv \sqrt{\overline{v_x^2}+\overline{v_y^2}}$, is shown in Figs. 5(c) and 5(g) for the nonreacting and reacting cases, respectively. Fluctuations of the velocity components in $x$ and $y$ directions are denoted, respectively, by $v_x$ and $v_y$. It is to be noted that there is no turbulence generating device in the burner, and the fluctuations in the velocity field are generated by the gradient production mechanism. The nonreacting flow result is as expected from classical fluid dynamic theory: The two shear layers, where the fluctuations are generated via gradient production mechanism, enclose a region of relatively low level of turbulence. This feature of the flow is clearly represented by the presence of a double peak in Fig. 6(c) for $y=10$ mm. This figure also shows the variation of $q$ along $x$ for four different $y$ locations. The double peak in the cold flow slowly disappears because of turbulent diffusion and thus the peak value of $q$ also decreases with $y$. The value of $q$ at the centerline, which is inside the recirculation region, increases. All of these features are clearly observable in Fig. 6(c). It is obvious that the double shear layer structure disappeared in the reacting case and $q$ inside the jetlike region is generally increased as in Fig. 5(g), which is clearly visible in Fig. 6(c). If one considers the jetlike region as the flame brush, which is debatable, then the effects of intermittency of the flame front location can explain the observed increase in $q$. However, inside the recirculation zone the turbulence is suppressed due to heat release effects as suggested by the results in Figs. 5(c), 5(d), 5(g), 5(h), and 6(c). A similar behavior is observed for other cases considered in this study.

### 2. Length and time scales of turbulence

Turbulence involves a spectrum of length and time scales. The heat release effects are expected to influence these scales, but the degree of influence will depend on the relative magnitude of turbulence and flame scales. If the turbulence scales are smaller than the flame scales, this corresponds to $\mathrm{Da}<1$ and $\mathrm{Ka}>1$ in terms of Damköhler and Karlovitz numbers, then the effect of heat release may not be felt by the turbulence. In the other limit of $\mathrm{Da}>1$ and $\mathrm{Ka}<1$, the effect of heat release will be felt by the whole spectrum of turbulence scales. Thus, one can naturally expect that the heat release may not affect certain size of scales if $\mathrm{Da}>1$ and $\mathrm{Ka}>1$. Here, it will be shown that the heat release affects all scales of turbulence.

Figure 7 shows typical two point correlation function for the axial velocity fluctuation $v_y$ from the flame FA1. The results are shown for both reacting and nonreacting cases for two different locations. $\Delta y=0$ in Figs. 7(a) and 7(b) correspond to (−10 and 20 mm) and (−15 and 25 mm), respectively, in terms of $x$ and $y$ locations. For the nonreacting case these two locations correspond to the edges of the shear layers, and for the reacting case, the first point is in the recirculation region while the second point is inside the flame brush (see Fig. 5). The variation of correlation coefficient shown in Fig. 7 for the cold flow is typical for PIV measurements and agrees with previous studies.[48,49] From these correlation functions, the integral length scales for the cold flow is estimated to be about 3.0 mm at (−10 and 20 mm) and 2.1 mm at (−15 and 25 mm). The corresponding values for the reacting case are 7.4 and 8.7 mm, which is close to the flame brush thickness estimate from the results in Fig. 6. Strictly, one needs mean temperature or a progress variable profile to calculate the flame brush thickness. There is a two- to fourfold increase in the local integral length scale due to heat release effects, which is consistent with earlier observations.[48] As noted earlier, the rms of velocity fluctuations generally increases in the presence of flame due to its intermittency. Thus, the flame effect on the integral time scale $(\Lambda/u')$ of the turbulence is determined by the combined influences on $\Lambda$ and $u'$. The analysis of the experimental data shows that the turbulence integral time scales in the reacting cases are about two to three times the cold flow values. If one uses the lateral correlation to obtain the inte-

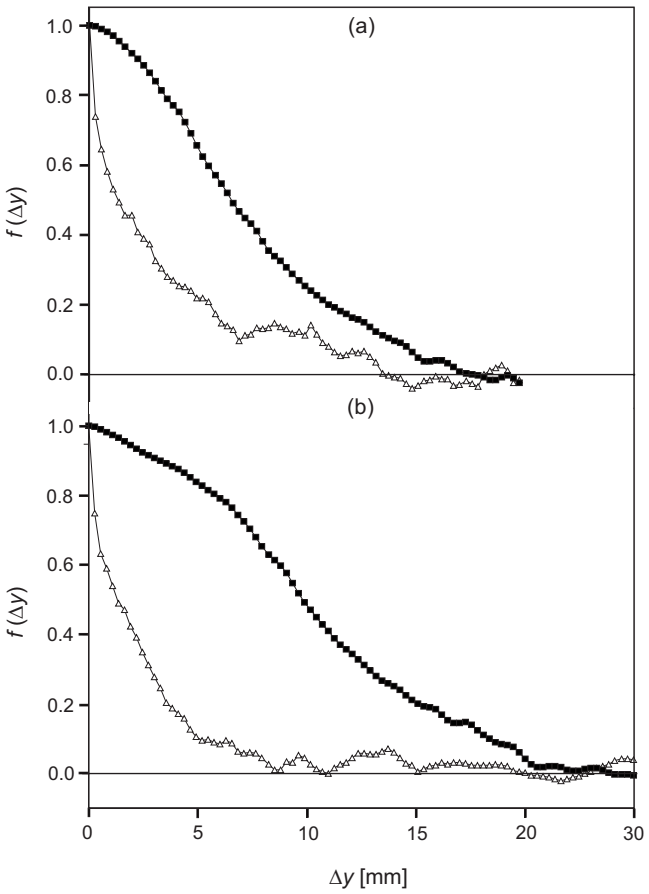


FIG. 7. Typical variation of the correlation function $f(\Delta y)$ in reacting (■) and nonreacting (△) cases. The results are shown for the flame FA1. $\Delta y = 0$ corresponds to the location $x=-10$ mm and $y=20$ mm in Fig. 5 for (a) and $x=-15$ mm and $y=25$ mm for (b).

gral length or time scale then a similar observation is also made. This might imply that the flame does not have a preferential direction, in an integral sense, to impart its influence on the fluid dynamics in the flow and burner configuration investigated here.

The results in Fig. 7 also indicate that the Taylor scale, which is related to the curvature of the correlation function at $\Delta y=0$, increases in the reacting cases. However, the influence of the flame on the Kolmogorov scales is slightly tricky to understand as it involves both the kinematic viscosity $\nu$ and the turbulence quantities which are influenced by the heat release. By differentiating the natural logarithm of the definitions of Kolmogorov time $t_\eta$ and length $\eta$ scales, one obtains

$$\frac{\Delta t_\eta}{t_\eta} = 0.5\frac{\Delta \nu}{\nu} + \mathcal{F} \quad \text{and} \quad \frac{\Delta \eta}{\eta} = 0.75\frac{\Delta \nu}{\nu} + 0.5\mathcal{F}, \tag{4}$$

where $\mathcal{F} \equiv 0.5(\Delta\Lambda/\Lambda) - 1.5(\Delta u'/u')$, by comparing the nonreacting and reacting cases. From the experimental results, $\mathcal{F}$ is calculated to be about 2.3 (spatially averaged) and note that $\mathcal{F}$ contains only the turbulence quantities including the flame front intermittency. Using a power law expression for the temperature dependence of the kinematic viscosity, $(\Delta\nu/\nu) = 1-(1+\tau)^{1.7} \simeq -20$, when $\tau \simeq 5$ (see Table I). Thus, it seems that the influence of the flame on the small scales of turbulence is felt predominantly (nearly an order of magnitude larger) via the molecular viscosity change, which is understandable since the Kolmogorov scales are the dissipative scales. It should, however, be cautioned here that the local temperature is not measured in the experiments and $(\Delta\nu/\nu) \simeq 20$ is only an estimate. Also $\mathcal{F}$ is observed to have a value as high as 18 locally in all the flames investigated here. It is interesting to note that this value is comparable to the estimate of the kinematic viscosity effects. It would be interesting to study the relative roles of those two effects through the use of simultaneous temperature measurement. Also, it is to be noted that the velocity fluctuation in the reacting case includes the effect of flame front intermittency and thus it is imperative that this effect is captured in the correlation function $f(\Delta y)$ shown in Fig. 7 and $\mathcal{F}$ in Eq. (4).

### 3. Velocity gradients

The velocity gradients play important role on flame front and turbulence dynamics and their mutual interactions. In the classical analysis of turbulent premixed flames, the influence of the velocity gradient on the flame front dynamics appears via the stretch factor or the Karlovitz number.[50] Even in strained laminar flames, the local velocity gradients are observed to play a significant role.[51] Equation (1) clearly shows the important role played by the strain rate tensor $e_{ij}$ on the evolution of the local mixing rate.

Figure 8 shows the PDF of the strain tensor components for the nonreacting and reacting cases corresponding to the flame FA1. Three out of nine components of the strain tensor are shown in Fig. 8 because only four components, $e_{xx}$, $e_{yy}$, $e_{xy}$, and $e_{yx}$, are available from the experiments, and the strain tensor is symmetric. For the cold flow case, the local Kolmogorov time scale is used to normalize the strain rates, whereas planar laminar flame time is used to normalize the strain rate in the flame case. The Kolmogorov time scale is obtained via $\hat{t_\eta} \simeq (\nu_u \Lambda/u'^3)^{1/2}$, where $u' \equiv \sqrt{\overline{v_x^2}+\overline{v_y^2}+\overline{v_z^2}}$. If one knows the local Karlovitz number Ka, then it is straight forward to go from one normalization to the other via, for example, $e_{xx}^+ = e_{xx}^* \mathrm{Ka}$, where the superscripts $+$ and $*$ denote the normalization using the planar flame scale and the Kolmogorov scale, respectively. The typical local values of Ka on the flame surface are observed to vary between 3 and 12 in the flames investigated here [see Fig. 9(a)]. The results in Fig. 8 are shown in a semilogarithmic plot to emphasize the tails of the PDFs. If there is local isotropy in small scales, then one would expect all three PDFs to fall close to each other, as has been observed by Mullin and Dahm.[29] The PDFs here are very different to each other and they have different statistical measures as noted in Table II, where the mean, the rms $\sigma$, the skewness $S$, and the kurtosis $K$, for the strain tensor components are given. For a Gaussian PDF $S=0$ and $K=3$. The values in Table II show that the PDFs shown in Fig. 8 for the nonreacting case are not truly Gaussian. This is because of the complex nature of the flow due to the presence of shear layers, recirculation eddy, stagnation planes, etc. It should be noted that the PDFs in Fig. 8 are constructed using the complete data sets without delineating the regions of the flow with strong and weak (or no) shears.

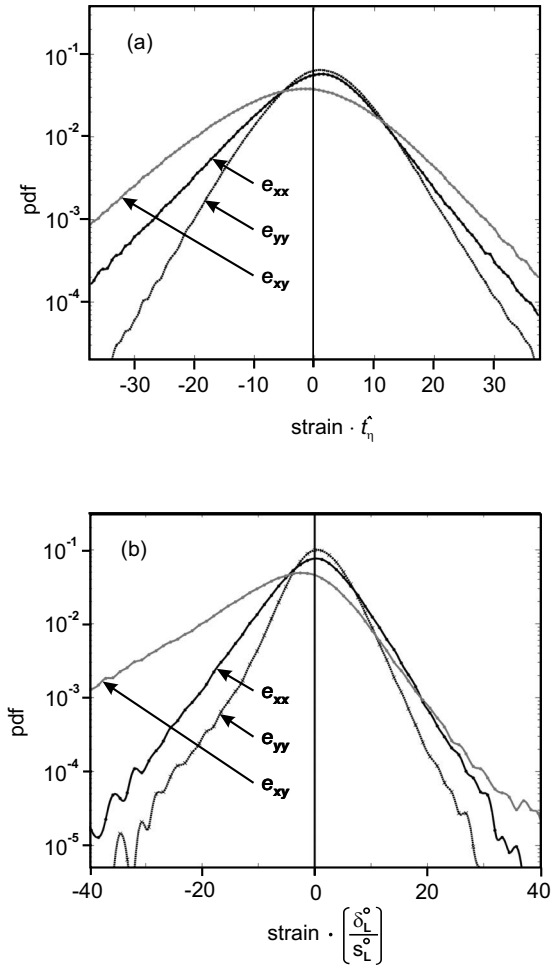


FIG. 8. Typical PDF of strain rate tensor $e_{ij}$ components for the flame FA1 and the corresponding cold flow; (a) nonreacting, (b) reacting.

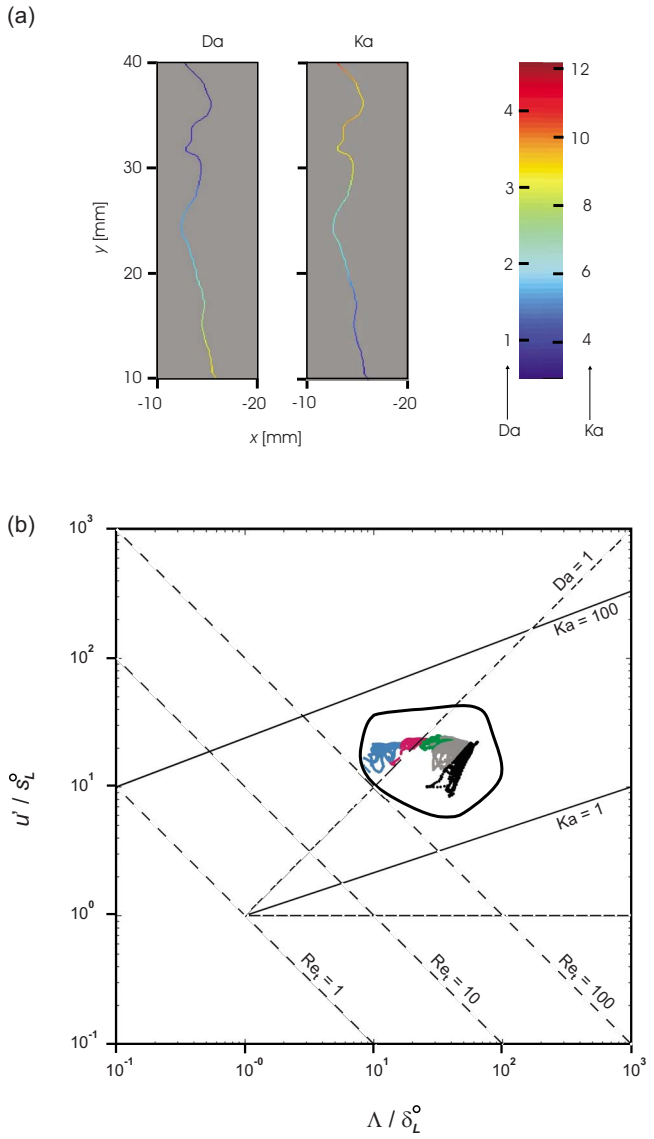


FIG. 9. (Color online) (a) Variation of local Da and Ka along the flame front (single OH-PLIF image) of the flame FA1. (b) The envelope of local combustion conditions in the five flames investigated. The dots show the combustion regime specifically for the flame FA1 as five equispaced regions along $y$ (see Fig. 5). The black color corresponds to $10 \leqslant y \leqslant 16$, while the light grey (blue online) color corresponds to $34 < y \leqslant 40$. The value of $y$ increases from black to light grey (blue).

It is known that the shear plays an important role on the behavior of these PDFs.[29] Since the interest here is to understand the influence of heat release on the behavior of the strain rate in an averaged sense, sheared and nonsheared flow regions were not distinguished in the analysis. However, this result is found to be consistent with earlier observations[29] after considering the presence of shear and other complexities in the flow.

Figure 8(b) shows the PDFs for a reacting case and the strain rate is normalized using the planar laminar flame time. The statistical characteristics for the reacting case, FA1, are given in Table II. The mean and rms values given in the table are normalized using the average Kolmogorov time scale, and they are obtained via $e_{ij}^+ = e_{ij}^* \overline{\mathrm{Ka}}$ using the mean Karlovitz number $\overline{\mathrm{Ka}}$ given in Table I. It is clear that the mean and rms values are reduced by an order of magnitude because of the dilatation caused by the flame. However, the strong acceleration caused by the flame imparts due influences on the local velocity gradients, and these effects have appeared via the higher moments of the strain rates. The increase in the negative skewness for $e_{xx}$ is caused by of the flow reversal, which leads to a high negative velocity gradient, as noted in Fig. 6(a). The values of $S$ and $K$ given in Table II for the reacting case indicate that the flame strongly influences the velocity gradient in the $x$ direction, which goes across the flame brush (see Fig. 5). This observation is consistent with what one would expect from the physics of turbulent premixed flames. Observations similar to those discussed above are also noted for the other flames studied. However, it should be pointed out that the relative changes in, rather than the absolute values of, various measures given in Table II are of interest to this study.

The discussion presented above clearly demonstrates the effects of dilatation on the dynamics of large and small scale fluid motions. These influences will obviously also affect the scalar mixing characteristics. The predominant influence is expected to come via the interaction of turbulence and the scalar field in the premixed flame, and this interaction pro-

TABLE II. Typical effect of heat release on the mean, standard deviation ($\sigma$), skewness ($S$), and kurtosis ($K$) of the strain tensor components. The strain rate is normalized by the Kolmogorov scale $\hat{t_\eta}$ and the values given below are for the flame FA1 and the corresponding cold flow.

| Component | Statistics | Nonreacting | Reacting |
|---|---|---|---|
| | Mean | 0.24 | 0.03 |
| $e_{xx}$ | $\sigma$ | 7.85 | 0.91 |
| | $S$ | −0.20 | −0.44 |
| | $K$ | 3.60 | 5.34 |
| | Mean | 1.02 | 0.12 |
| $e_{yy}$ | $\sigma$ | 7.05 | 0.55 |
| | $S$ | 0.01 | 0.14 |
| | $K$ | 3.32 | 3.60 |
| | Mean | −2.60 | 0.78 |
| $e_{xy}$ | $\sigma$ | 10.00 | 1.38 |
| | $S$ | 0.09 | −1.12 |
| | $K$ | 2.62 | 5.36 |

cess involves the gradients of flow and scalar fields as noted in Eq. (1). Our attention will focus on this interaction in the next section.

## B. Flame related quantities

### 1. Combustion regime

Before discussing the results on the turbulence-scalar interaction process, the regime of turbulent combustion in the present experiments is established. It is traditional practice in experimental studies of turbulent premixed flames to quote values of Da and Ka based on the upstream turbulence condition, usually taken at the center of the burner nozzle exit or based on a cold flow characterization of the burner. This can be an oversimplification from the combustion modeling point of view, since the dynamics of turbulence-flame interaction is dictated by the local competition between the fluid dynamic and chemical processes.[19] Furthermore, it was noted in the previous section that the local flow quantities can significantly change due to dilatational effects. It should be remarked that the values of local Da and Ka are readily available in turbulent flame computations since the evolution equations for turbulence quantities are solved. Thus, it is believed that providing the local values of Da and Ka, if they can be obtained, from turbulent flame experiments would be of immense value to model development and to further our understanding of turbulence-flame interaction. It was shown in the previous section that the local turbulence quantities were measured with an uncertainty of a few percent using stereoscopic PIV, and hence one can easily estimate the local Da and Ka values. These values are shown in Fig. 9(a) for a typical flame. The Damköhler number is large near the burner and decreases as one moves downstream along the instantaneous flame contour, whereas the Karlovitz number shows the opposite trend. The observed behavior is due to the change in turbulence characteristics although the entrainment of ambient air can alter the stoichiometry in the downstream regions. If one considers this effect also, then the spread noted in Fig. 9(b) will shift further into low Da region. The behavior noted in Fig. 9 is expected, but the important point to note is that the local flame dynamics can change significantly as one travels downstream and thus combustion submodels should include local Da and Ka in order to capture the dynamics of turbulence-chemistry interaction correctly.

A representative value for the Damköhler number can be obtained by averaging the Da shown in Fig. 9(a) over the 75 images acquired and also spatially. These averaged values are given in Table I as $\overline{\mathrm{Da}}$ and $\overline{\mathrm{Ka}}$ for all of the five flames, which are typical of combustion in thin reaction zone regime.[21] If one plots the local values of Da and Ka on the combustion regime diagram then there will be a cloud of data points, as shown in Fig. 9(b). Five different colors are used to denote five spatial regions along the streamwise, $y$, direction. The thick black line encloses the entire data from all of the five flames investigated in this study, and the complete data are within the thin reaction zone regime of Peters.[21] However, one should note that a considerable portion of the data has $\mathrm{Da}<1$, which can be classified as distributed combustion regime[52] since the integral scales of turbulence are smaller than the planar laminar flame scales.

From the OH-PLIF image used to identify the flame fronts, one can extract the curvature of the fronts as noted in Sec. II C 3. The PDF of flame curvature (not shown) peaks at $k\delta_L^o=0$ implying that the flame brush is statistically planar and the PDF value at $k\delta_L^o=\pm 0.5$ drops almost symmetrically to about one-tenth of its peak value for all the five flames investigated here. The PDF becomes almost zero at $k\delta_L^o=\pm 1$ which is similar to that observed in DNS studies.[53]

### 2. PDF of principal strain rates

Since the prime interest here is to investigate the alignment of the flame surface with the principal strain rates, the PDFs of these strain rates for the reacting cases were studied first. The results for the nonreacting cases are discussed earlier. Figure 10 shows the PDF of the compressive, $e_1$, and the extensive, $e_2$, principal strain rates. Note that there are only two principal strain rates because the velocity gradient in $z$ direction is unavailable. If one uses a dual plane stereoscopic PIV, then it is possible to obtain all three principal strain rates, this will form a part of future work. However, this limitation is less likely to influence the qualitative features of these PDFs and the other results to be presented below. This is because the flow is evolving in 3D space, and thus the instantaneous velocities measured and the four components of the strain rate tensor calculated naturally include the due effects of the velocity gradient in $z$ direction on the dynamics of turbulence, flame, and their mutual interaction. One can, however, expect some quantitative changes that may not alter the conclusions drawn from the present results. Some support to this argument is also provided later by analyzing DNS data.[54]

The PDFs of the principal strain rates for the turbulent flames FA1, FA2, and FC1 are shown in Figs. 10(a)–10(c), respectively. The strain rates are normalized using the corresponding planar laminar flame scales. As noted earlier, only

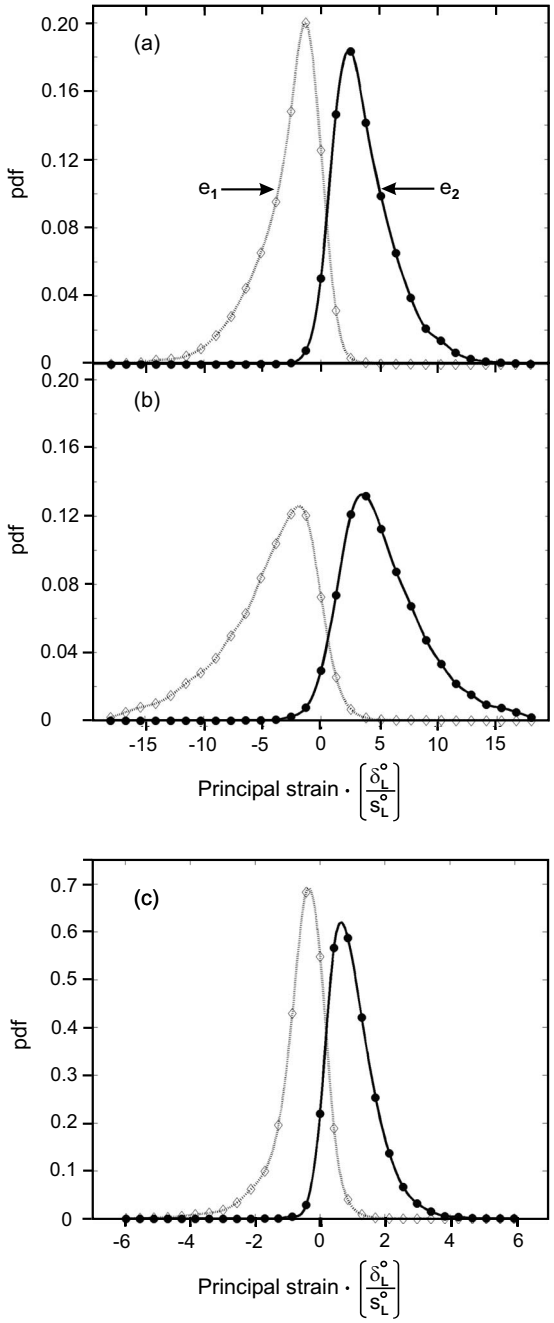


FIG. 10. PDF of principal strain rates, $e_1$ and $e_2$, in the turbulent flames (a) FA1, (b) FA2, and (c) FC1. The principal strains are normalized using the corresponding planar laminar flame scales.

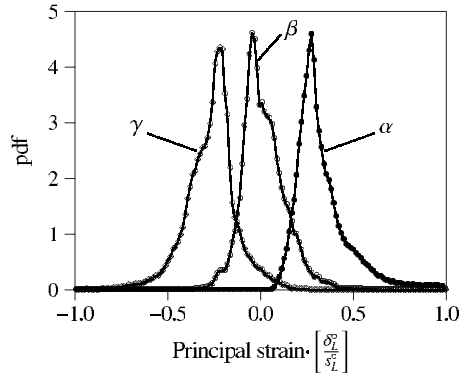


FIG. 11. PDF of principal strain rates, $\alpha$, $\beta$, and $\gamma$, in a typical reacting region of a DNS flame (Ref. 54) The principal strains are normalized using the planar laminar flame scales.

two eigenvalues of the strain tensor matrix are available from the measured quantities. As one would expect, the range of these eigenvalues increases as the turbulence Reynolds number increases, which is indicated by the broader PDFs in Fig. 10(b) compared to those in Fig. 10(a). Also, the most probable eigenvalues normalized using the laminar flame time increase from $e_1=-1.3$ and $e_2=2.5$ in the flame FA1 to $e_1=-1.7$ and $e_2=3.5$ in the flame FA2. If the reactivity in the flame is increased by increasing the stoichiometry as in flame FC1, then the range of normalized principal strain rates acting on the flame surface is reduced by nearly 60% as in Fig. 10(c). This is because of the strong dilatational effects. A typical scaling for the dilatation is either $\tau$Da, if one uses the integral scales of the turbulence, or $\tau/\mathrm{Ka}$, if the Kolmogorov scales are used, to normalize the dilatation. The flame FC1 has high $\overline{\mathrm{Da}}$ and low $\overline{\mathrm{Ka}}$ as noted in Table I, and thus the local dilatation is strong leading to a reduction in the influence of fluid mechanical processes on the flame front. Consequently, the principal strain rates acting on the flame surface are reduced as in Fig. 10(c), which also shows that the most probable values of $e_1$ and $e_2$ are −0.5 and 0.63, respectively. These values are smaller than the values for the flame FA1, which has the same Re as the flame FC1. The average values of $e_1$ and $e_2$ also decrease as $\overline{\mathrm{Da}}$ increases. As one would expect, the average values of $e_1$ and $e_2$ increase with Re. A close inspection of Fig. 10 also reveals that the peak values of $e_1$ and $e_2$ PDFs differ by about 10%, this difference is deemed to be statistically insignificant by comparing it to the experimental accuracy, which is estimated to be about 8%. The crossing of PDFs shown in Fig. 10 around the zero value for the normalized strain rate is consistent with earlier DNS studies.[18,55]

Figure 11 shows the PDFs of the three principal strain rates, normalized using the corresponding laminar flame scales, from a DNS flame[54] with Da=6.8 and Ka=0.3 at the start of the simulation. This flame has been used in a number of earlier investigations, for example, see Refs. 18 and 19. The typical PDFs in Fig. 11, extracted from a location inside the DNS flame brush where the Favre averaged mean progress variable is about 0.23, show attributes which are consistent with the PDFs obtained from the experiment. The most probable principal strain rate in the DNS case is lower than $(s_L^o/\delta_L^o)$ because of the low Re of the simulation. It is also to be noted that the presence of the intermediate principal strain rate $\beta$ in the analysis simply separates the PDFs of the other two eigenvalues (the size of the overlapping region around zero is reduced). This is confirmed by calculating the eigenvalues $e_1$ and $e_2$ of the submatrix of the strain tensor matrix from the DNS flame. Thus, it is believed that the conclusions drawn from this work are less likely to be limited by the absence of the third eigenvalue in the analysis.

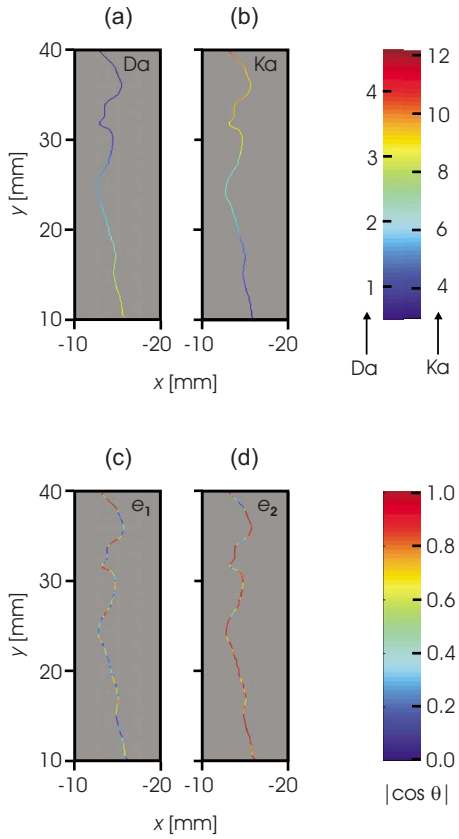


FIG. 12. (Color online) Variation of local (a) Da and (b) Ka along the flame front (constructed from a single shot) of the flame FA1. The flame normal alignment with the (c) compressive and (d) extensive eigenvectors.

### 3. Flame surface alignment with principal strain rates

Equation (1) shows that the influence of turbulence on the evolution of the scalar gradient magnitude comes via the inner tensor product of scalar gradient vector and the strain tensor. Thus, the alignment between the flame normal vector and the eigenvectors of the strain tensor plays an important role. This alignment has been investigated in earlier studies using DNS flames with the laminar flame scales either larger or smaller than all the relevant scales of turbulence.[6,19] These studies showed that the gradient vector is more likely to align with the most extensive strain rate when $\overline{\mathrm{Da}}>1$ and $\overline{\mathrm{Ka}}<1$. Such an alignment is observed in the regions of intense heat release when $\overline{\mathrm{Da}}<1$ and $\overline{\mathrm{Ka}}>1$, showing a strong influence of the dilatation or the chemical strain rate on the flame front dynamics.

The local alignment characteristics are obtained using the eigenvectors of the strain tensor matrix and the flame normals, obtained as discussed in Sec. II C 3. A typical result is shown in Fig. 12 where the local values of Da and Ka are also given. Figure 12(c) shows the magnitude of the cosine of the angle between the flame normal and the compressive eigenvector $e_1$, whereas Fig. 12(d) shows the result for the extensive eigenvector $e_2$. The values in these two figures are unsmoothed. The increased tendency for the flame normal to align with the extensive strain rate is very clear. The role of local competition between the chemical and fluid dynamic process is also clear near $y=40$ mm, where $\mathrm{Da}<1$ and the flame normal aligns with the compressive eigenvalue $e_1$. Furthermore, the curvature, irrespective of its sign, is observed to play a role and more detail on this point will be discussed in the next subsection.

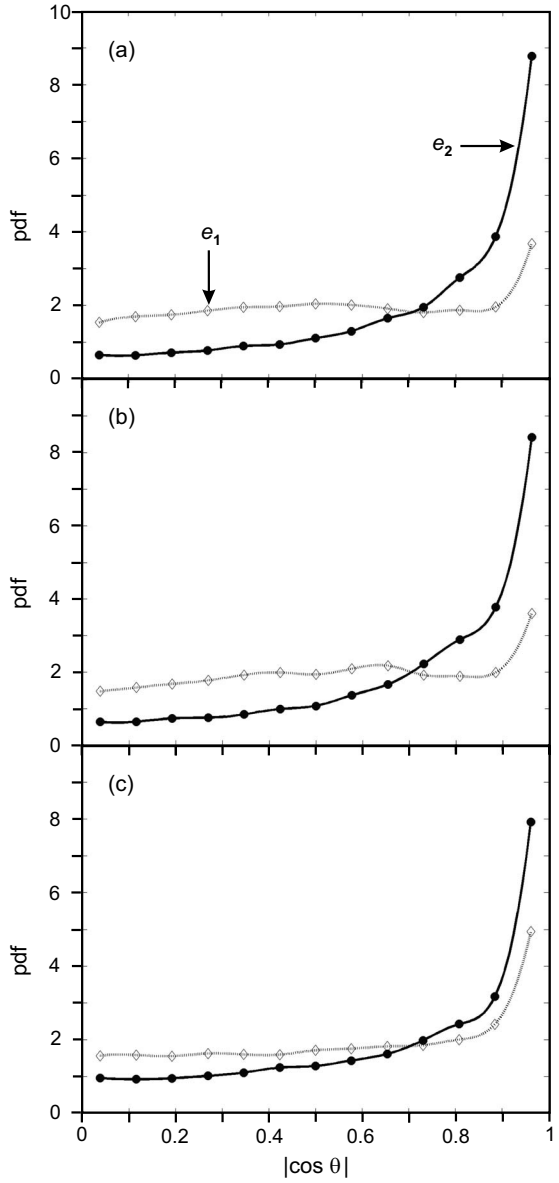


FIG. 13. PDF of flame normal alignment with the principal strain rates, $e_1$ the compressive strain rate, and $e_2$ the extensive strain rate, for the flames (a) FA1, (b) FA2, and (c) FB1.

Using several of the instantaneous images shown in Figs. 12(c) and 12(d), one can construct the PDFs of the flame normal alignment. These PDFs are shown in Fig. 13 for the flames FA1, FA2, and FB1. The PDFs shown contain more than 2500 samples in each bin. The preferential alignment of the flame normal with the most extensive strain rate is again clear, and this alignment is observed for all the cases considered here. The increase in the alignment PDF for the compressive strain near $|\cos\theta|\simeq 0.9$ may be due to the absence of the third eigenvalue and its vector in the analysis. However, it is to be noted that the PDF for the alignment with the extensive principal strain rate is nearly two and half

TABLE III. Ratio $\mathcal{R}$ of the peaks of alignment PDFs, conditioned on flame curvature, of extensive to compressive principal strain rates; $k$: curvature in $mm^{-1}$.

| | FA0 | FA1 | FA2 | FB1 | FC1 |
|---|---|---|---|---|---|
| $\mathcal{R}$ (unconditioned) | 2.1 | 2.4 | 2.3 | 2.4 | 1.6 |
| $\mathcal{R}$ ($k=-1.0\pm0.2$) | 1.3 | 1.4 | 1.1 | 1.5 | 1.2 |
| $\mathcal{R}$ ( $k=0.0\pm0.2$)) | 2.8 | 2.7 | 3.0 | 3.0 | 1.8 |
| $\mathcal{R}$ ( $k=+1.0\pm0.2$)) | 1.4 | 2.0 | 1.2 | 1.3 | 1.2 |

times larger than that for the compressive principal strain rate. It is quite likely that this factor would increase further if the third eigenvalue should be included in the analysis. However, this needs to be proven via further experiments.

### C. Discussion

Using the results above and that published recently,[18,19] one can say that the scalar gradients preferentially align with the extensive principal strain rate in turbulent premixed flames with Damköhler numbers greater than unity. Note that the flame FA2 with $\overline{\mathrm{Da}}=1$, see Table I, also shows the alignment with the extensive strain rate. This alignment implies that the isoscalar surfaces are pulled apart by the turbulence, thereby decreasing the scalar gradients. This gradient destruction is aided by molecular diffusion and dissipation, denoted by the first and second terms on the right hand side of Eq. (1), while the scalar gradients are produced by the chemical reactions. This was noted in earlier studies[18,19] with laminar flame scales either larger or smaller than the relevant scales of turbulence. The results shown here suggest that those physical phenomena also occur in turbulent flames with $\mathrm{Da}>1$ and $\mathrm{Ka}>1$. The destruction of scalar gradient by the turbulence observed in premixed flames is caused by strong influence of dilatation on turbulence dynamics. Thus, the use[56] of exponential growth of a strained interface, representing the flame, area in kinematic modeling of turbulent premixed flames is not justified as the exponential growth model is based on passive scalar turbulence, where the scalar gradients are produced by the turbulence via pushing the isoscalar surfaces together by the most compressive principal strain.[7] The influence of dilatation is usually considered to be important only when the rms of the turbulent velocity fluctuation is less than or equal to three times the planar laminar flame speed,[50,57] but here the influence of dilatation on the alignment characteristics, thus on the small scale quantities, is observed to persist even at $u'/s_L^o \simeq 40$. It is also well known that the behavior of small scale quantities dictates the behavior of large scale quantities.[58] Thus, carrying over the scaling laws and the physics of passive scalar turbulence to the modeling of turbulent premixed flames cannot be justified fully and it can lead to potential pitfalls.

A popular approach to model turbulent premixed flame is based on the kinematics of a propagative surface.[21] In this approach, the mean curvature of the flame surface appears as an important parameter, and thus one can ask if the curvature of the flame front plays a role in the alignment characteristic observed above. It was already noted in Fig. 12 that the curvature indeed plays a role on the alignment characteristics. Explanation to this dependence can readily be obtained from the existing knowledge in literature[53,59] and using the dilatation equation.[6] This equation gives

$$\nabla \cdot \mathbf{u} = \frac{\tau}{\rho_u}(\dot{\omega}_c + \nabla \cdot \rho\kappa \nabla c) = \tau\frac{\rho}{\rho_u}|\nabla c|S_d, \tag{5}$$

relating the instantaneous dilatation, the gradient of $c$, and the displacement speed $S_d$. The later two quantities are known to correlate negatively with the magnitude of flame curvature.[59] Thus, the dilatation is expected to have a negative correlation with the curvature magnitude, and so the influence of the dilatation on the dynamics of scalar-turbulence interaction may become reduced in strongly curved regions. Hence, one may expect a reduction in the tendency of the flame normal to align with the extensive principal strain rate, which is noted in Fig. 12. The alignment PDFs conditioned on the flame front curvature are similar to that shown in Fig. 13 with peaks near $|\cos\theta| \simeq 1$. The ratio $\mathcal{R}$ of the peak value of this conditioned PDF for the alignment with the extensive principal strain rate to that for the compressive principal strain rate is given in Table III. It is clear that there is significant reduction in the alignment PDF for the extensive principal strain rate. Such a change with curvature is also noted in a study using DNS data.[60] However, it is to be noted that the ratio $\mathcal{R}$ is always greater than 1, implying that the turbulence dissipates the scalar gradients even in strongly curved regions in an average sense. The combustion submodels or a model for the turbulent burning velocity should include the physics implied by the alignment characteristics since this characteristics dictate the physics of scalar mixing.

## IV. SUMMARY AND CONCLUSION

The influence of dilatation on the dynamics of turbulence and scalar-turbulence interactions in premixed flames has been studied via experimental methods. Five turbulent premixed ethylene-air flames, stabilized by a bluff body and located in the thin reaction zones regime,[50] were investigated using simultaneous OH-PLIF and SPIV techniques. The dynamics and geometrical characteristics of the flame front were captured by the OH-PLIF technique, while SPIV provides the local fluid dynamic information. Care was taken to ensure that the laser sheets for OH-PLIF and SPIV passed through exactly the same plane of measurement, and also that the PLIF and PIV images were aligned pixel by pixel before extracting any quantitative information from the measurement. The flame front was tracked using the Canny edge

detection algorithm[41] by detecting the maximum gradient of OH. A local third order polynomial was used to represent the flame front in order to obtain the flame curvature and its normal. The velocities obtained from the SPIV images were differentiated using Richardson extrapolation scheme to get the strain rates $e_{ij}$. Since a single laser sheet was used for SPIV measurement, only four out of nine components of $e_{ij}$ were available for analysis. Two eigenvalues, a compressive and an extensive one, were obtained from the strain tensor matrix at every pixel location. The informations on the mean velocities, rms velocities, length and time scales of turbulence, and velocity gradients were extracted for both the cold and hot flows. The flame normal and the eigenvectors obtained at every pixel were coprocessed to study their alignment.

The heat release from the turbulent flame strongly affects the shape, size, and the characteristics of the recirculation region behind the bluff body. The strong shear, $\partial V_z/\partial x$, presented in the cold flow case is damped by the dilatation. The strong acceleration of the flow across the flame and the outward shift of the stagnation plane of the recirculating eddy yields a negative cross stream velocity in the reacting cases. These results are consistent with previous studies.[26,47] The rms of velocity fluctuations within the flame brush is observed to be larger than the corresponding cold flow values because of the intermittency in the flame front location. The length and time scales of the turbulence are increased by the heat release as one would expect. The predominant influence, on an average, of heat release on the Kolmogorov scale is noted to come via the temperature dependence of the molecular viscosity. However, the local influence of heat release on the Kolmogorov scale via the dilatational effects on turbulence can be comparable to the molecular viscosity effect. The mean and rms of velocity gradients are reduced in the reacting flows for a given Reynolds number. The local flow acceleration created by the flame front can skew the velocity gradient PDFs and it can increase the kurtosis of these PDFs.

The dynamics of the scalar-turbulence interaction in premixed flames is observed to be completely different from that of passive scalar turbulence. The flame normal is observed to have high tendency to align with the extensive principal strain rate which implies that the scalar gradients are destroyed by the turbulence via pulling the isoscalar surfaces apart. This is contrary to the passive scalar turbulence case, where the turbulence generates the scalar gradient by pushing the isoscalar surfaces together. Thus, the use of passive scalar mixing models for turbulent premixed flames is not valid. The above observations are consistent with DNS studies,[18,19] involving turbulent premixed flames having laminar flame scales either larger or smaller than the relevant scales of turbulence. In this study, the turbulent flames have large Reynolds number and Damköhler and Karlovitz numbers which are typical of many practical flames. Based on the results in Refs. 18 and 19 and in the current study, one can conclude that the turbulence destroys the scalar gradient in premixed flames if Da is large. This finding is contrary to common practice followed in turbulent premixed flame modeling. It must, however, be remarked here that the present analysis involves only two eigenvalues because of current experimental limitations. It is expected that the presence of a third eigenvalue in the analysis is less likely to alter the above conclusion. Another point to note is that the effect of dilatation is persistent even at $u'/s_L^o \simeq 40$. Thus the combustion submodels and models for the turbulent burning velocity should include the dilatational effects appropriately. The flames considered here have Lewis numbers close to unity. It would be interesting to see if the same alignment persists also for other Lewis numbers.

## ACKNOWLEDGMENTS

We would like to thank Professor M. R. Mackley for the loan of the PIV system. We are also grateful to Dr. T. Nickels for help with the PIV software.

This work was supported by grants from the EPSRC and grants from EU's Sixth Framework Programme INTELLECT D.M. contract (EU Project AST3-CT-2003-502961, 01 January 2004–31 December 2007). G.H. is grateful to a case studentship from CMI (Cambridge-MIT Institute) and INTELLECT D.M. J.H. was supported by an Advanced Research Fellowship from the EPSRC (EP/C012399/1). C.F.K. is thankful to the Leverhulme trust for personal sponsorship. The support of EPSRC is acknowledged by J.R. and N.S.

[1] D. Bradley, P. H. Gaskell, and X. J. Gu, "Application of a Reynolds stress, stretched flamelet, mathematical model to computations of turbulent burning velocities and comparison with experiments," Combust. Flame **96**, 221 (1994).
[2] A. Y. Klimenko and R. W. Bilger, "Conditional moment closure for turbulent combustion," Prog. Energy Combust. Sci. **25**, 595 (1999).
[3] S. B. Pope, "Computations of turbulent combustion: Progress and challenges," Proc. Combust. Inst. **23**, 591 (1990).
[4] K. N. C. Bray, *Turbulent Reacting Flows* (Springer-Verlag, New York, 1980), pp. 115–183.
[5] P. A. Libby and K. N. C. Bray, "Implications of the laminar flamelet model in premixed turbulent combustion," Combust. Flame **39**, 33 (1980).
[6] N. Swaminathan and K. N. C. Bray, "Effect of dilatation on scalar dissipation in turbulent premixed flames," Combust. Flame **143**, 549 (2005).
[7] G. Batchelor, "The effect of homogeneous turbulence on material lines and surfaces," Proc. R. Soc. London, Ser. A **231**, 349 (1952).
[8] G. Batchelor, "Small scale variations of convected quantities like temperature in turbulent fluid, part 1. General discussion and the case of small conductivity," J. Fluid Mech. **5**, 113 (1959).
[9] C. Gibson, "Fine structure of scalar fields mixed by turbulence. I. Zero gradient points and minimal gradient surfaces," Phys. Fluids **11**, 2305 (1968).
[10] J. P. Clay, Ph.D. thesis, University of California, San Diego, 1973.
[11] R. M. Kerr, "Higher-order derivative correlations and the alignment of small-scale structures in isotropic numerical turbulence," J. Fluid Mech. **153**, 31 (1985).
[12] W. T. Ashurst, A. Kerstein, R. Kerr, and C. Gibson, "Alignment of vorticity and scalar gradient with strain rate in simulated Navier–Stokes turbulence," Phys. Fluids **30**, 2342 (1987).
[13] G. Ruetsch and M. Maxey, "Small-scale features of vorticity and passive scalar fields in homogeneous isotropic turbulence," Phys. Fluids A **3**, 1587 (1991).
[14] K. Nomura and S. Elghobashi, "Mixing characteristics of an inhomogeneous scalar in isotropic and homogeneous sheared turbulence," Phys. Fluids A **4**, 606 (1992).
[15] A. Garcia and M. Gonzalez, "Analysis of passive scalar gradient alignment in a simplified three-dimensional case," Phys. Fluids **18**, 058101 (2006).
[16] W. T. Ashurst, N. Peters, and M. D. Smooke, "Numerical simulation of turbulent flame structure with non-unity Lewis number," Combust. Sci. Technol. **53**, 339 (1987).
[17] C. J. Rutland and A. Trouvé, "Direct simulation of premixed flames with non-unity Lewis numbers," Combust. Flame **94**, 41 (1993).

[18]N. Swaminathan and R. W. Grout, "Interaction of turbulence and scalar fields in premixed flames," Phys. Fluids **18**, 045102 (2006).
[19]N. Chakraborty and N. Swaminathan, "Influence of Damköhler number on turbulence-scalar interaction in premixed flames. I. Physical insight," Phys. Fluids **19**, 045103 (2007).
[20]N. Chakraborty and N. Swaminathan, "Influence of Damköhler number on turbulence-scalar interaction in premixed flames. II. Model development," Phys. Fluids **19**, 045104 (2007).
[21]N. Peters, *Turbulent Combustion* (Cambridge University Press, Cambridge, 2000).
[22]B. Ayoola, "Laser-based measurement of heat release rate and temperature in turbulent premixed flames," Ph.D. thesis, University of Cambridge (2006).
[23]R. Balachandran, B. O. Ayoola, C. F. Kaminski, A. P. Dowling, and E. Mastorakos, "Experimental investigation of the nonlinear response of turbulent premixed flames to imposed inlet velocity oscillations," Combust. Flame **143**, 37 (2005).
[24]B. O. Ayoola, R. Balachandran, J. H. Frank, E. Mastorakos, and C. F. Kaminski, "Spatially resolved heat release rate measurements in turbulent premixed flames," Combust. Flame **144**, 1 (2006).
[25]R. Balachandran, "Experimental investigation of the response of turbulent premixed flames to acoustic oscillations," Ph.D. thesis, University of Cambridge (2006).
[26]M. V. Heitor, A. M. K. P. Taylor, and J. H. Whitelaw, "The interaction of turbulence and pressure gradients in a baffle-stabilized premixed flame," J. Fluid Mech. **181**, 387 (1987).
[27]W. Wang and B. Rogg, "Premixed ethylene/air and ethane/air flames: reduced mechanisms based on inner iteration," in *Reduced Kinetic Mechanisms for Applications in Combustion Systems*, edited by N. Peters and B. Rogg (Springer Verlag, Berlin, 1993), pp. 76–101.
[28]T. Hirasawa, C. J. Sung, A. Joshi, Z. Yang, H. Wang, and C. K. Law, "Determination of laminar flame speeds using digital particle image velocimetry: binary fuel blends of ethylene, n-butane, and toluene," Proc. Combust. Inst. **29**, 1427 (2002).
[29]J. A. Mullin and W. J. A. Dahm, "Dual-plane stereo particle image velocimetry measurements of velocity tensor fields in turbulent shear flow. II. Experimental results," Phys. Fluids **18**, 035102 (2006).
[30]Y.-C. Chen and R. W. Bilger, "Simultaneous 2-D imaging measurements of reaction progress variable and OH radical concentration in turbulent premixed flames: Instantaneous flame front structure," Combust. Sci. Technol. **167**, 187 (2001).
[31]Y.-C. Chen and R. W. Bilger, "Experimental investigation of three-dimensional flame front structure in premixed turbulent combustion-I: hydrocarbon/air Bunsen flames," Combust. Flame **131**, 400 (2002).
[32]H. N. Najm, P. H. Paul, C. J. Mueller, and P. S. Wyckoff, "On the adequacy of certain experimental observables as measurements of flame burning rate," Combust. Flame **113**, 312 (1998).
[33]P. S. Kothnur, M. S. Tsurikov, N. T. Clemens, J. M. Donbar, and C. D. Carter, "Planar imaging of CH, OH, and velocity in turbulent nonpremixed jet flames," Proc. Combust. Inst. **29**, 1921 (2002).
[34]R. Giezendanner, O. Keck, P. Weigand, W. Meier, U. Meier, W. Stricker, and A. Aigner, "Periodic combustion instabilities in a swirl burner studied by phase-locked planar laser-induced fluorescence," Combust. Sci. Technol. **175**, 721 (2003).
[35]R. J. H. Klein-Douwel, J. B. Jeffries, J. Luque, G. P. Smith, and R. Crosley, "CH and formaldehyde structures in partially-premixed methane/air coflow flames," Combust. Sci. Technol. **167**, 291 (2001).
[36]P. H. Paul and H. N. Najm, "Planar Laser-Induced Fluorescence imaging of flame heat release rate," Proc. Combust. Inst. **27**, 43 (1998).
[37]J. E. Rehm and P. H. Paul, "Reaction rate imaging," Proc. Combust. Inst. **28**, 1775 (2000).
[38]F. Scarano and M. L. Riethmuller, "Iterative multigrid approach in PIV image processing with discrete window offset," Exp. Fluids **26**, 513 (1999).
[39]K. Jambunathan, X. Y. Ju, B. N. Dobbins, and S. Ashforth-Frost, "An improved cross-correlation technique for particle image velocimetry," Meas. Sci. Technol. **6**, 507 (1995).
[40]H. Malm, G. Sparr, J. Hult, and C. F. Kaminski, "Nonlinear diffusion filtering of images obtained by planar laser-induced fluorescence spectroscopy," J. Opt. Soc. Am. A **17**, 2148 (2000).
[41]J. Canny, "A computational approach to edge-detection," IEEE Trans. Pattern Anal. Mach. Intell. **8**, 679 (1986).
[42]R. J. Kee, J. F. Grcar, M. D. Smooke, and J. A. Miller, "A FORTRAN program for modelling steady laminar one-dimensional premixed flames," Sandia National Laboratories Report No. SAND85-8240 (1993).
[43]S. Gashi, J. Hult, K. W. Jenkins, N. Chakraborty, R. S. Cant, and C. Kaminski, "Curvature and wrinkling of premixed flame kernels—comparison of OH-PLIF and DNS data," Proc. Combust. Inst. **30**, 809 (2005).
[44]H. Stöcker, *Taschenbuch der Physik*, 3rd ed. (Verlag Harri Deutsch, Frankfurt am Main, 1998).
[45]M. Raffel, C. Willert, and J. Kompenhans, *Particle Image Velocimetry* (Springer, Berlin, 1998).
[46]J. A. Mullin and W. J. A. Dahm, "Dual-plane stereo particle image velocimetry measurements of velocity gradient tensor fields in turbulent shear flow. I. Accuracy assessments," Phys. Fluids **18**, 035101 (2006).
[47]N. Swaminathan and B. Dally, "Cross stream dependence of conditional averages in elliptic region of flows behind a bluff-body," Phys. Fluids **10**, 2424 (1998).
[48]Y.-C. Chen, N. Peters, G. Schneemann, N. Wruck, U. Renz, and M. S. Mansour, "The detailed flame structure of highly stretched turbulent premixed methane-air flames," Combust. Flame **107**, 223 (1996).
[49]Y.-C. Chen and R. W. Bilger, "Turbulence measurements on a Bunsen burner inserted with perforated plugs of different hole sizes using DPIV," Exp. Therm. Fluid Sci. **27**, 619 (2003).
[50]N. Peters, H. Wenzel, and F. A. Williams, "Modification of the turbulent burning velocity by gas expansion," Proc. Combust. Inst. **28**, 235 (2000).
[51]T. Hirasawa, C. J. Sung, A. Joshi, Z. Yang, H. Wang, and C. K. Law, "Determination of laminar flame speeds using digital particle velocimetry: Binary fuel blends of ethylene, n-butane and toluene," Proc. Combust. Inst. **29**, 1427 (2002).
[52]M. Summerfield, S. H. Reiter, V. Kebely, and R. W. Mascolo, "The structure and propagation mechanism of turbulent flames in high speed flow," Jet Propul. **25**, 377 (1955).
[53]N. Chakraborty and R. S. Cant, "Unsteady effects of strain rate and curvature on turbulent premixed flames in an inflow-outflow configuration," Combust. Flame **137**, 129 (2004).
[54]C. J. Rutland and R. S. Cant, "Turbulent transport in premixed flames," in *Proceedings of the Summer Program* (Center for Turbulence Research, Stanford, 1994), p. 75.
[55]S. Zhang, "Direct numerical simulations of premixed turbulent flames with variable density," Ph.D. thesis, University of Wisconsin-Madison (1994).
[56]A. Kerstein, "Simple derivation of Yakhot's turbulent premixed flamespeed formula," Combust. Sci. Technol. **60**, 163 (1988).
[57]N. Peters, "The turbulent burning velocity for large-scale and small-scale turbulence," J. Fluid Mech. **384**, 107 (1999).
[58]N. Swaminathan, R. W. Bilger, and G. R. Ruetsch, "Interdependence of the instantaneous flame front structure and the overall scalar flux in turbulent premixed flames," Combust. Sci. Technol. **128**, 73 (1997).
[59]N. Chakraborty and R. S. Cant, "Effects of strain rate and curvature on surface density function transport in turbulent premixed flames in the thin reaction zones regime," Phys. Fluids **17**, 065108 (2005).
[60]S. H. Kim and H. Pitsch, "Scalar gradient and small-scale structure in turbulent premixed combustion," Phys. Fluids **19**, 115104 (2007).